IJMMM International Journal of Minerals, Metallurgy and Materials 矿物冶金与材料学报（英文版）

Coupling effect of the conductivities of Li ions and electrons by introducing LLTO@C fibers in the $LiNi_{0.8}Co_{0.15}Al_{0.05}O_2$ cathode

Hao-yang Wang, Xue Cheng, Xiao-feng Li, Ji-min Pan, and Jun-hua Hu

Cite this article as:
Hao-yang Wang, Xue Cheng, Xiao-feng Li, Ji-min Pan, and Jun-hua Hu, Coupling effect of the conductivities of Li ions and electrons by introducing LLTO@C fibers in the $LiNi_{0.8}Co_{0.15}Al_{0.05}O_2$ cathode, *Int. J. Miner. Metall. Mater.*, 28(2021), No. 2, pp. 305-316. https://doi.org/10.1007/s12613-020-2145-6

View the article online at SpringerLink or IJMMM Webpage.

International Journal of Minerals, Metallurgy and Materials
Volume 28, Number 2, February 2021, Page 305
https://doi.org/10.1007/s12613-020-2145-6

Coupling effect of the conductivities of Li ions and electrons by introducing LLTO@C fibers in the $LiNi_{0.8}Co_{0.15}Al_{0.05}O_2$ cathode

Hao-yang Wang[1,2,3], *Xue Cheng*[1,2], *Xiao-feng Li*[1,2], *Ji-min Pan*[1], *and Jun-hua Hu*[1,2,3]

1) School of Materials Science and Engineering, Zhengzhou University, Zhengzhou 450001, China
2) State Center for International Cooperation on Designer Low-carbon & Environmental Materials (CDLCEM), Zhengzhou University, Zhengzhou 450001, China
3) Zhengzhou Materials Genome Institute (ZMGI), Xingyang 450100, China
(Received: 25 May 2020; revised: 12 July 2020; accepted: 15 July 2020)

Abstract: To probe the coupling effect of the electron and Li ion conductivities in Ni-rich layered materials ($LiNi_{0.8}Co_{0.15}Al_{0.05}O_2$, NCA), lithium lanthanum titanate (LLTO) nanofiber and carbon-coated LLTO fiber (LLTO@C) materials were introduced to polyvinylidene difluoride in a cathode. The enhancement of the conductivity was indicated by the suppressed impedance and polarization. At 1 and 5 C, the cathodes with coupling conductive paths had a more stable cycling performance. The coupling mechanism was analyzed based on the chemical state and structure evolution of NCA after cycling for 200 cycles at 5 C. In the pristine cathode, the propagation of lattice damaged regions, which consist of high-density edge-dislocation walls, destroyed the bulk integrity of NCA. In addition, the formation of a rock-salt phase on the surface of NCA caused a capacity loss. In contrast, in the LLTO@C modified cathode, although the formation of dislocation-driven atomic lattice broken regions and cation mixing occurred, they were limited to a scale of several atoms, which retarded the generation of the rock-salt phase and resulted in a pre-eminent capacity retention. Only NiO phase "pitting" occurred. A mechanism based on the synergistic transport of Li ions and electrons was proposed.

Keywords: Ni-rich cathode; coupling mechanism; dislocation wall; coaxial structure; cation mixing

1. Introduction

The depletion of traditional fuel resources and aggravation of environmental challenges have recently led to a boost in the development of new energy. The development of lithium ion batteries (LIBs), which possess a high specific capacity and working voltage, an excellent cycle stability, and environmental friendliness, has led to unprecedented opportunities for a new generation of electric vehicles and plug-in hybrid electric vehicles [1–6]. The capacity of cathodes has always been the decisive factor that hinders further improvement in the capacity of LIBs. In all types of current cathodes, the layered Ni-rich cathode $LiNi_{0.8}Co_{0.15}Al_{0.05}O_2$ (NCA) has attracted the attention of researchers because of its high specific power density, low cost, and toxicity, and it has gradually become the most promising cathode material [7–11]. However, the capacity attenuation caused by the poor structural stability of the material during cycling has hindered the further commercialization of NCA cathodes. The capacity loss is derived from the structure degradation from the layered structure (R-3m space group) to the spinel structure (Fd3m) and ultimately to the rock-salt structure (Fm-3m) [12–16]. The generation of the rock-salt phase is considered a severe factor resulting in a drastic performance fading. Meanwhile, the generation of oxygen gas from the surface of NCA directly accelerates the degradation of the structure and increases the explosibility [17].

The transportation of electrons and Li ions plays a crucial role during the process of establishing a fluent cycling from $LiNiO_2$ to $Li_{1-x}Ni^{3+/2+}O_{2-y}$ [18–19]. During the delithiation process, Ni ions would be oxidized from Ni^{3+} to Ni^{4+}, which is thermodynamically metastable and could be easily reduced to Ni^{2+} [20−21]. The reduced Ni^{2+} would slide to the interstitial sites of NCA, resulting in cation mixing [22−23]. During the lithiation process, the localized cation mixing is reversible with the intercalation of Li^+ and oxidation of Ni^{2+}. If the transportation of Li^+ or electrons is blocked, the transition of $Li_{1-x}Ni^{3+/4+}O_2$ to $Li_{1-x}Ni^{3+/2+}O_{2-y}$ would not be fully reversible [19,24]. In such a case, the accumulated cation mixing will cause the generation of the rock-salt structure, which accounts for the capacity loss of NCA upon cycling [25]. The evolution of oxygen from the NCA lattice was caused by the

Corresponding author: Jun-hua Hu E-mail: hujh@zzu.edu.cn

insufficient compensation of Li ions and charge [17]. To address these problems, fast ion conductors have been used as active additions in the cathode. Coating methodologies are commonly adopted to enhance the performance of NCA. Various solid electrolytes or oxides, such as $LiZr_2(PO_4)_3$ [26], $Li_{0.5}La_{0.5}TiO_3$ [27], LiPON [28], Li_2O–ZrO_2 (LZO) [29], $LiMnPO_4$ [30], Li_2SiO_3 [31], Li_2MnO_3 [21], $CeVO_4$ [32], Co_3O_4 [33], Al_2O_3 [34], and SnO_2 [35] have been intensively applied to construct core-shell structures to provide a sufficient Li^+ diffusion "shell" and solid "clothes" to support active materials. Alternatively, a full gradient cathode was developed by doping $Li_{6.75}La_3Zr_{1.75}Ta_{0.25}O_{12}$ (LLZTO), and a localized cation migration region was generated in NCA, which hindered the further distortion of the crystal structure and enhanced the capacity retention [36]. The construction of a full gradient cathode also proved the significance of optimizing the kinetics environment of the entire NCA cathode [27]. Lithium lanthanum titanate ($Li_{3x}La_{2/3-x}TiO_3$, denoted LLTO) exhibits excellent Li^+ conductivity, a wide electrochemical window and good thermal stability. Therefore, it has been investigated as a fast ion conductor oxide solid electrolyte. At the same time, it is a modifying material for enhancing the Li transport kinetics of the cathode [27,36]. The straight LLTO nanofiber can provide a continuous and rapid conductivity path of lithium ions. Theoretically, it is not sufficient to construct only a Li ion diffusion path in a cathode. However, reports on the coupling of ion and electron transport in a cathode are few. We are motivated to propose the application of LLTO@C nanofiber in the NCA cathode, which can achieve a synergy of Li^+ and e− conductivity.

However, as indicated by the reaction process of Ni ions, similar to both sides of a coin, the reversibility is not only determined by the ion transport process but also by the electron process [18–19,37−39]. The investigation of the coupling mechanism between the transport of Li ions and electrons was not as sufficient as that of some novel types of batteries [40]. In this work, we propose a prototype cathode configuration to demonstrate the coupling mechanism of Li ions and electrons to enhance the reversibility via the addition of $Li_{0.35}La_{0.55}TiO_3$@C (LLTO@C) nanofibers to the cathode of NCA, by which the kinetics condition and phase transition process are regulated. As expected, the modified NCA cathode presents a profoundly enhanced electrochemical performance during high-rate cycling.

2. Experimental

2.1. Synthesis of LLTO@C nanofibers

The LLTO nanofibers were prepared by electrospinning and subsequent calcination processes. A precursor consisting of lithium nitrite ($LiNO_3$, 2.01 mmol), lanthanum nitrite hexahydrate ($La(NO_3)_3{\cdot}6H_2O$, 2.75 mmol), tetrabutyl titanate ($Ti(OC_4H_9)_4$, 5 mmol), and an appropriate amount of polyvinylpyrrolidone (PVP) was dissolved in a uniform solution containing a mixture of N, N-dimethylformamide (DMF, 12 mL), ethanol (C_2H_5OH, 10 mL), and glacial acetic acid (CH_3COOH, 4 mL). In particular, an excess of 15wt% $LiNO_3$ was provided to compensate for the Li loss during the sintering process. The precursor solution was stirred for 12 h until a pale yellow homogeneous solution was obtained. Then, the precursor solution was loaded into a 10 mL hypodermic syringe and injected from a stainless steel needle to a rolling collector (50 r/min) at a −5 kV voltage. A positive voltage of 15 kV was applied to the stainless steel needle. The syringe piston was pushed ahead at a rate of 1 mm/min. The spinning needle was controlled at a distance of 15 cm from the collecting drum. The as-spun nanofibers were collected and sintered at 850°C in air for 3 h at a heating rate of 5°C/min to remove the organic components and crystallize the LLTO. A typical example of this electrostatic spinning process is provided in the literature [41−43].

The prepared nanofibers and glucose ($C_6H_{12}O_6$) in a mass ratio of 1: 5 were placed in a Teflon-lined stainless steel autoclave with a 100-mL capacity that contained 60 mL of deionized water (DW). After vigorous stirring for 10 min, a suspension was obtained. The autoclave was sealed and treated at 180°C for 5 h in an oven. After heating, the suspension was centrifuged and cleaned with DW four times and desiccated at 80°C for 8 h. Finally, the as-obtained sample was sintered at 600°C for 2 h in a vacuum furnace (0.1 Pa) to achieve carbonization. The sample was denoted LLTO@C.

2.2. Battery assembly and electrochemical measurements

The electrochemical performance was measured in a CR2025-type coin cell. The as-prepared LLTO@C nanofibers were added to the polyvinylidene difluoride (PVDF) binder at a weight ratio of 0, 10wt%, or 20wt%. To prepare the cathode slurry, the active material $LiNi_{0.8}Co_{0.15}Al_{0.05}O_2$ (NCA, MTI Corporation, Hefei), carbon black (Super C65, TIMACAL), and the PVDF binder (Arkema, Kynar 761) were mixed uniformly in an N-methyl-2-pyrrolidone (NMP, Aladdin) solvent in a weight ratio of 8:1:1. The slurry was vigorously stirred for 12 h to guarantee its uniformity, and was cast onto an aluminum foil (MTI Corporation, Hefei). After that, the electrodes were desiccated in a vacuum at 80°C for 12 h to remove the residual NMP. The electrode films were punched into disks with a diameter of 12 mm, and further desiccated at 100°C for 12 h in a vacuum. For convenience, the as-prepared cathodes were named according to the weight ratio of LLTO@C in the PVDF binder: NCA-pristine (0), NCA-10L@C (10wt%), and NCA-20L@C (20wt%). Cathodes with 20 wt% LLTO nanofibers in PVDF without carbon layers were also prepared and were denoted NCA-20L. The CR2025-type coin cells were assembled in a glove box filled with argon. The as-prepared cathode, Celgard 2300 film as the separator, and lithium metal anode were pressed together in that order. An electrolyte solution

with 1 mol of $LiPF_6$ dissolved in ethylene carbonate and ethylmethyl carbonate (EMC) (3:7 in volume) was used. Electrochemical impedance spectroscopy (EIS) and cyclic voltammetry (CV) were performed with a VMP3B-20 electrochemical workstation. The EIS measurement frequency ranged from 100 to 100 mHz with an ac amplitude of 5 mV at room temperature (RT). CV tests with different scan rates from 0.02 to 2 mV/s were performed. The charge and discharge profiles were recorded in the windows of 2.7–4.3 V and 2.7–4.5 V, respectively, vs Li/Li^+ at RT with a LANHE CT2001A battery system. All tested cells were activated at 0.1 C for 5 cycles (1 C = 200 $mA \cdot g^{-1}$).

3. Results and discussion

3.1. Characterization of the as-prepared LLTO@C nanofiber

The as-fabricated LLTO has a morphology of continuous fibers having a diameter of less than 100 nm (Fig. 1(a)). After the fibers are coated by carbon layers (Fig. 1(b)), the increasing diameter of the fibers indicates the uniformity of the carbon coating. LLTO and LLTO@C have similar ionic conductivity to $Li_{0.35}La_{0.55}TiO_3$ with cubic-phase primitive perovskite structure, which is more than 1×10^{-4} $S \cdot cm^{-1}$ at RT [44–47]. The TEM image of LLTO@C in Fig. 1(c) depicts a coaxial structure consisting of an inner LLTO nanofiber and an outer carbon layer. The thickness of the carbon layer is shown in the inset of Fig. 1(c). The carbon layer maintains a continuous and sharp interface with LLTO. In addition, the distribution of the elements in the LLTO@C nanofiber is analyzed by EDS mapping, as shown in Figs. 1(e)−1(i). This EDS mapping clearly shows that the C, La, Ti, and O elements are distributed uniformly. The distribution of C (Fig. 1(f)) is wider than that of the other elements, indicating that the C coating is uniform.

3.2. Coupling conductive effect in the $LiNi_{0.8}Co_{0.15}Al_{0.05}O_2$ cathode

The CR2025-type coin cells were assembled by coupling composite NCA cathodes with a Li anode. Fig. 2(a) compares their cycling performances for 200 cycles at 1 C in the voltage range of 2.7−4.3 V. The discharge capacity of NCA-pristine, NCA-10L@C, and NCA-20L@C is 101.3, 114.5, and 142.0 $mAh \cdot g^{-1}$ after 200 cycles, respectively. The NCA-20L@C cell possesses the highest capacity retention rate (77.2%), followed by NCA-10L@C (62.7%) and NCA-pristine (56.2%). Fig. 2(b) shows the variation trend of the medium voltage at the discharge plateau within 200 cycles. The NCA-20L@C maintains the highest discharge median voltage of ~ 3.698 V, while the NCA-pristine cell presents a

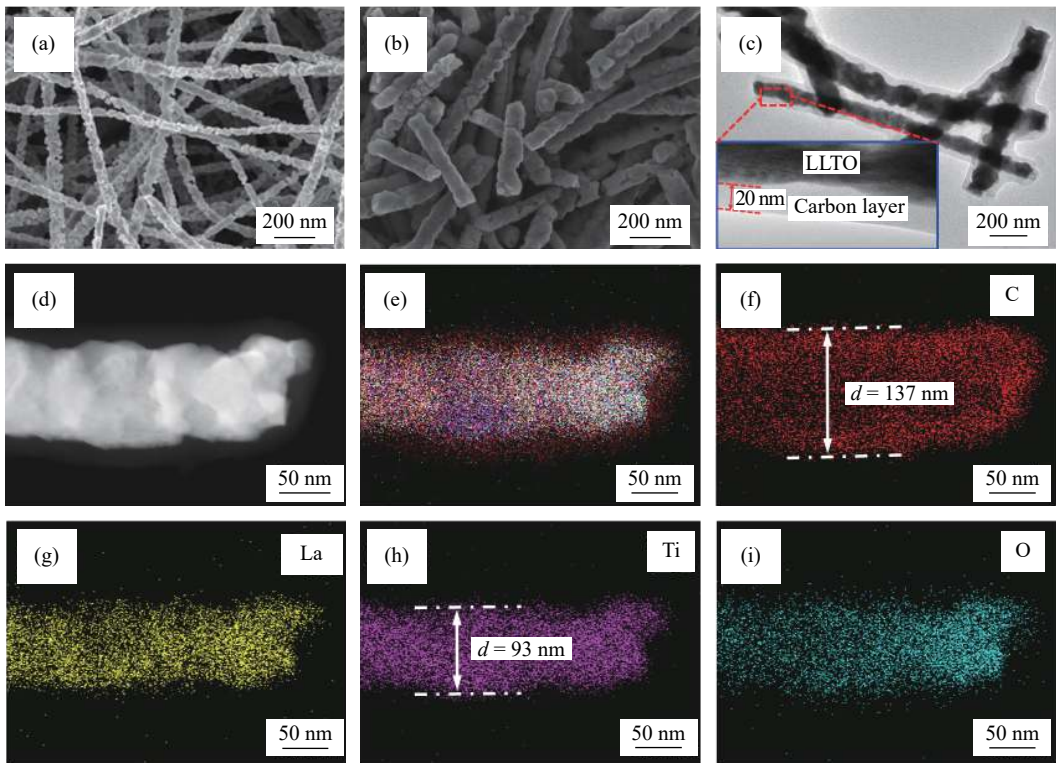

Fig. 1. Scanning electron microscope (SEM) images of the (a) as-fabricated LLTO nanofibers and (b) LLTO@C nanofibers. (c) TEM images of the LLTO@C nanofibers. The inset shows the magnified carbon layer and the LLTO@C interface. (d) High-angle annular dark field image of a selected LLTO@C nanofiber. (e) Overlapping image of the EDS mapping and corresponding distribution of C (f), La (g), Ti (h) and O (i). The "*d*" in (f) and (h) refers to the diameter of LLTO nanofiber.

more sluggish voltage drop (3.592 V) after 200 cycles. The NCA-10L@C cell is less promoted than NCA-20L@C. The drop in the voltage (Fig. 2(b)) is widely regarded to be closely related to the transition from the spinel phase to the layered phase by the migration of transition metal (TM) ions [26]. The voltage drop is effectively mitigated with the addition of LLTO@C. The inhibition of the voltage fading of NCA-20L@C is ascribed to the structural stability obtained by incorporating LLTO@C nanofibers. To better comprehend the remarkable cycling degradation that occurred during the long-term cycling of the NCA cathode, EIS before and after 200 cycles was additionally recorded, as shown in Figs. 2(c) and 2(d), respectively. In addition, the illustration in Fig. 2(c) shows the equivalent circuit T-model derived from the Nyquist plots. The EIS plots include a semicircle in the high- to intermediate-frequency region, which refers to the charge-transfer resistance (R_{ct}) of the electrochemical reaction, and the slope in the low-frequency region refers to the Warburg impedance (Z_w) of surface Li^+ ions diffusion [28,48]. The three cells present low resistance values before cycling (inset in Fig. 2(c)), which indicates a good contact between the interface and assembly. After 200 cycles, the impedance value R_{ct} of NCA-pristine increases from 89.72 (1st) to 213.29 Ω (200th), suggesting that the resistance increases upon cycling. In contrast, the NCA-20L@C cell presents the lowest impedance change, indicating that the NCA-20L@C cathode can maintain the original structure and interface contact [26]. The inset of Fig. 2(d) presents the suppressive effect on the increasing electrochemical impedance in the high-frequency region for NCA-20L@C. The enhancement of the conductivity of Li^+ and electrons with the addition of LLTO@C was determined by the EIS evolution in the low- and high-frequency regions, respectively. In addition to the carbon layer on the fibers, the improvement is also related to the structural integrity, which well maintains electrical contact in the NCA particles.

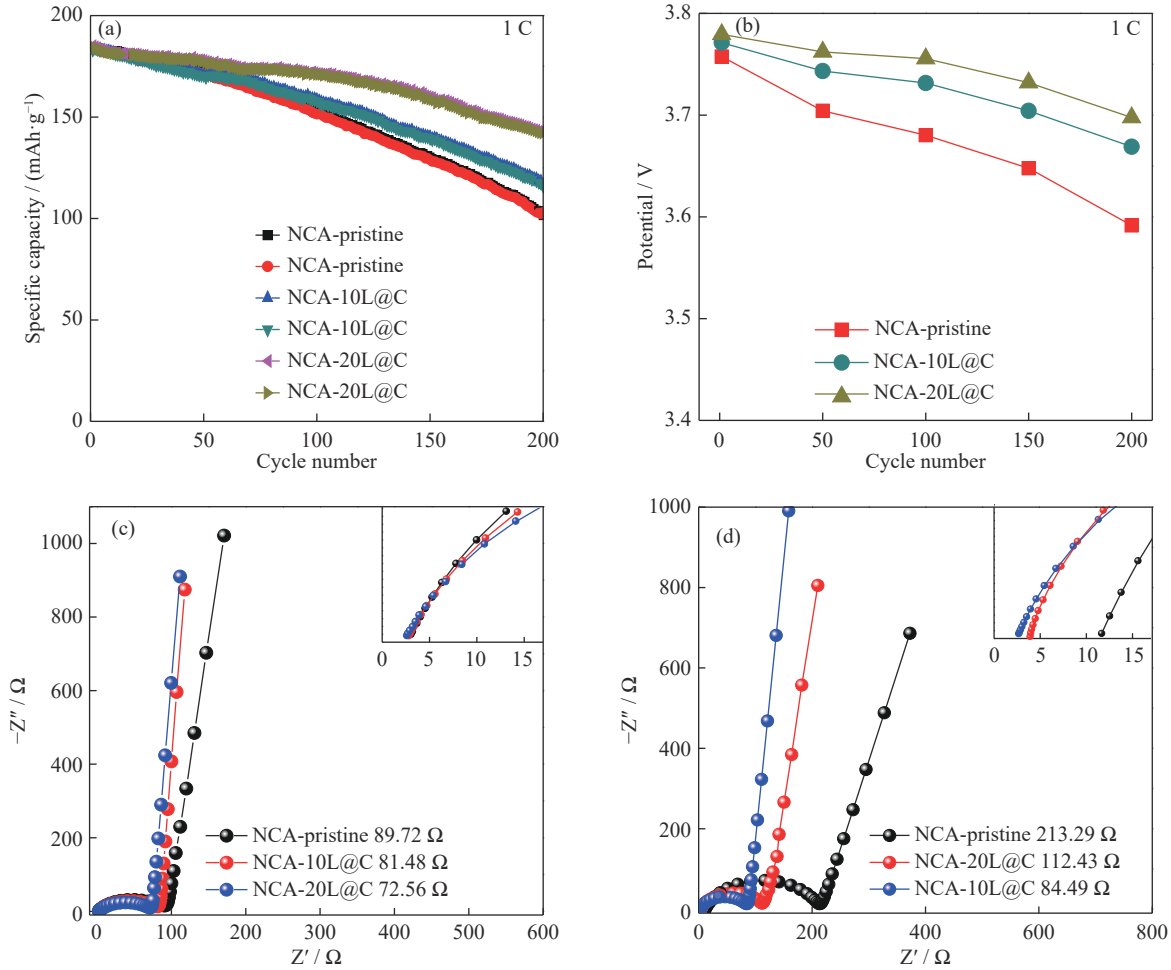

Fig. 2. Electrochemical performance of NCA-pristine, NCA-10L@C, and NCA-20L@C: (a) cycle performance at 1 C; (b) the variation trend of the medium voltage at the discharge plateau of the 1st, 50th, 100th, and 200th cycles within 200 cycles; EIS plots (c) before cycling and (d) after 200 cycles. The insets in (c) and (d) show the corresponding magnifications of the EIS plots in the high-frequency (100 kHz) region.

CV curves were studied and the detailed information on the redox behavior correlating with the phase transition was obtained. Figs. 3(a) and 3(b) show the initial three cycles performance at 2.7–4.3 V for the NCA-pristine and NCA-20L@C samples, respectively. In the positive scan of the first cycle, both samples show three anodic peaks, which are caused by the phase transitions from hexagonal to monoclinic (H_1 to M), monoclinic to hexagonal (M to H_2), and hexagonal to hexagonal (H_2 to H_3) during the Li ions extraction process [22,30]. The locations of the first anodic peaks for NCA-pristine and NCA-20L@C are 3.65 and 3.71 V, respectively. An obvious decrease in polarization can be observed after the modification of NCA-20L@C. In particular, it was generally accepted that the phase transition from H_2 to H_3 at approximately 4.20 V would generate a large volume variation in the NCA cathode because of the significant difference in their lattice parameters [21,49]. In this phase transition process, a NiO_2 microregion would be generated, which is thermodynamically metastable and easily gives rise to the release of oxygen gas, ultimately leading to structural damage and capacity loss [21,50]. Comparing Fig. 3(a) with Fig. 3(b), it shows that the third anodic peak (4.20 V) assigned to the H_2–H_3 transition is suppressed distinctly. Moreover, the differences between the oxidation peak and reduction peak during the initial 3 cycles are quantified and shown in Table 1, which illustrates the degree of polarization. During the first cycle of CV, the difference between the main redox peaks (Δ1) of NCA-20L@C is 0.19 V, which is smaller than that of NCA-pristine (0.22 V). Notably, the potential differences between the redox peaks of NCA-20L@C during the second and third cycles drastically decrease to 0.02 and 0.01 V, respectively, compared with those of NCA-pristine. The further separation of the oxidation peaks shown in Fig. 3(a) suggests that the structure degradation has begun to accumulate in the NCA cathode without LLTO@C.

Additionally, to further investigate the promotion effect on the Li conductivity by LLTO@C addition to the cathode, a series of CV curves were obtained at scan rates ranging from 0.2 to 2 $mV \cdot s^{-1}$ for NCA-pristine and NCA-20L@C. As shown in Figs. 3(c) and 3(d), with increasing scan rate, the cathodic peaks shift to the lower potentials, and the anodic peaks shift to the higher potentials. Meanwhile, it shows the degree of polarization at different scan rates, in which the suppressed polarization by the modification of LLTO@C is apparent. The peak current of the CV curve is proportional to the square root of the scan rate ($v^{1/2}$) and can be expressed by

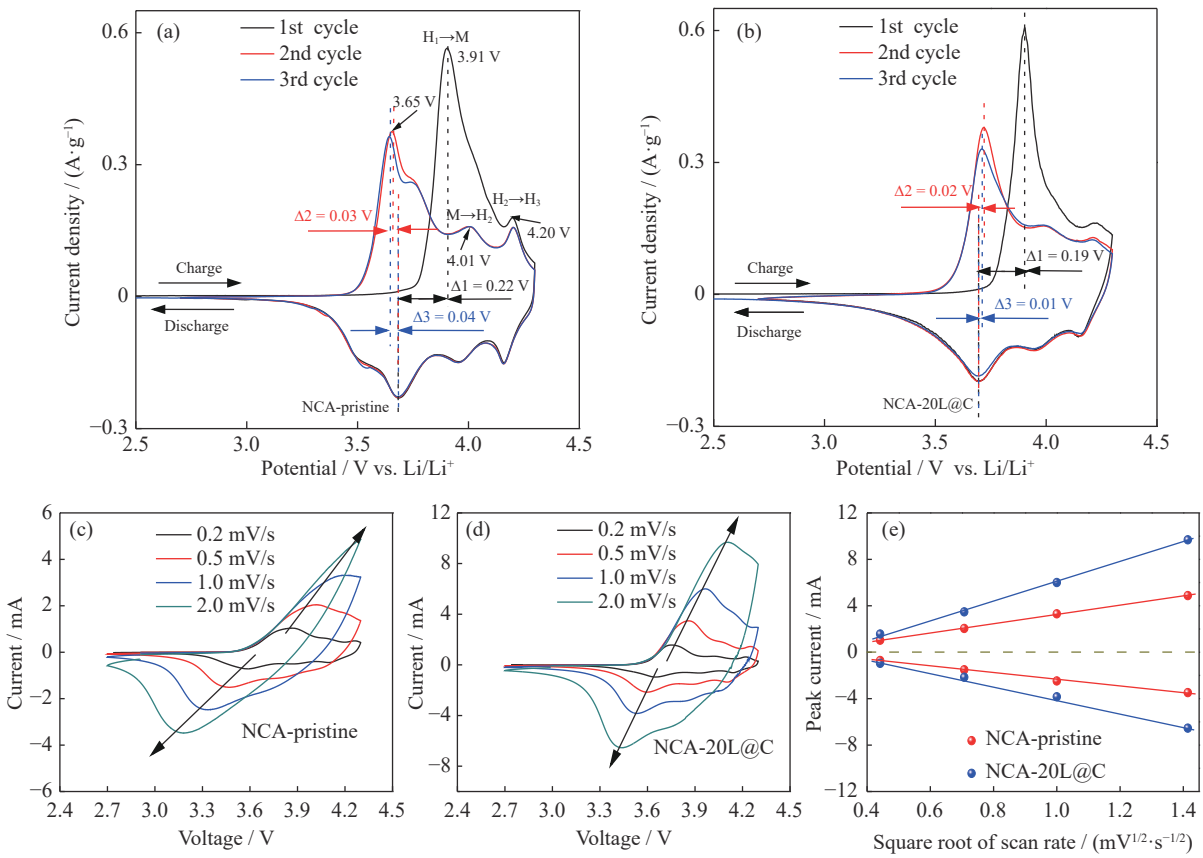

Fig. 3. CV curves of (a) NCA-pristine and (b) NCA-20L@C during the initial three cycles performed at a rate of 0.05 mV/s. CV curves of (c) NCA-pristine and (d) NCA-20L@C obtained with different scan rates. (e) The relationship between the peak current (I_p) and $v^{1/2}$ of NCA-pristine and NCA-20L@C.

Table 1. Values of the potential interval for the NCA-pristine and NCA-20L@C samples V

Number	NCA-pristine	NCA-20L@C
Δ1	0.22	0.19
Δ2	0.03	0.02
Δ3	0.04	0.01

the Randles–Sevcik equation, from which the diffusion coefficient (D_{Li+}) of NCA-pristine and NCA-20L@C can be estimated [26,30,51]. The linear relationship between I_p and $v^{1/2}$, shown in Fig. 3(e), indicates that the reaction kinetics of the NCA cathode is controlled by the diffusion process [30]. As presented in Table 2, the calculated D_{Li+} value of NCA-20L@C (7.661×10^{-10} cm^2·S^{-1}) is higher than that of NCA-pristine (1.714×10^{-10} cm^2·S^{-1}), indicating the enhanced Li^+ diffusion coefficient and kinetics resulting from modification with LLTO@C, which is consistent with the results of EIS.

Table 2. CV testing detail parameters used for NCA-pristine and NCA-20L@C samples

Sample	D_{Li+} (charge) / (cm^2·S^{-1})	D_{Li+} (discharge) / (cm^2·S^{-1})
NCA-pristine	1.714×10^{-10}	2.079×10^{-11}
NCA-20L@C	7.661×10^{-10}	3.626×10^{-10}

To verify the coupling effect between LLTO and the carbon layer, the cycling at 5 C and the rating performance of NCA-20L and NCA-20L@C were compared. As shown in Fig. 4(a), the NCA-20L@C cell maintains the highest capacity, 102.7 mAh·g^{-1}, and a capacity retention of 68.9% after 200 cycles, which is much higher than that of pristine NCA (only 40.2%). The NCA-20L sample, modified with bare LLTO fibers, delivers a moderate cycling performance with a capacity retention of 51.4%. The superior high-rate tolerance of NCA-20L@C is demonstrated through the long-term cycling at 5 C. Meanwhile, the rate capability of the three samples was also investigated and is shown in Fig. 4(b). The rates were increased from 0.1 to 5 C (1 C = 200 mA·g^{-1}), then decreased to 0.1 C. The increasing rates give rise to a gradually fading capacity because of the electrode polarization. It is apparent that the NCA-pristine cell exhibits an inferior rate performance, with a sharp decrease in the reversible capacity, especially at the high rate of 5 C, which results from the degraded structure and increased impedance (as shown in Figs. 2 and 3). The NCA-20L@C sample presents a superior rate ability and a stable discharge capacity (136.1 mAh·g^{-1}) at 5 C. When the rate gradually returns to 0.1 C, the capacity of NCA-20L@C recovers to the initial capacity level of 206.1 mAh·g^{-1}.

To explain the enhancement of the cell performance, the structure and chemical state evolutions were analyzed. An *ex situ* XRD test was conducted after 200 cycles at 5 C, as shown in Fig. 5(a). The NCA-pristine cathode shows an evident co-existence of the H_2 and H_3 phases after cycling. Meanwhile, the NCA-20L@C structure is most similar to the NCA structure before cycling [52–53]. XPS was used to analyze the chemical state of Ni in the NCA particle after cycling. In Figs. 5(b)–5(d), the two main peaks correspond to Ni $2p_{3/2}$ and Ni $2p_{1/2}$. The Ni $2p_{3/2}$ peaks of NCA-pristine, NCA-20L, and NCA-20L@C are located at 854.9, 855.1, and 855.4 eV, respectively. The higher binding energy indicates an enhancement of the nickel-oxygen bond. When the Ni cations slide to the Li sites, they are reduced and show a decrease in the Ni–O bond length [36,54–55]. In the deconvoluted Ni $2p_{3/2}$ peaks, the Ni^{2+} content of 15.80% for NCA-20L@C is much lower than those of NCA-20L and NCA-pristine, which are 18.95% and 25.12%, respectively. The modification by LLTO@C sustained the spinel structure and suppressed the cation mixing [32,56].

The SEM and HRTEM images of the NCA cathodes after cycling at 5 C were analyzed. Figs. 6(a) and 6(b) show the HRTEM image and corresponding fast Fourier transform (FFT) patterns of the regions in the bulk and surface of NCA, respectively, after 200 cycles at 5 C. In Fig. 6(a), the phase transition of NCA-pristine caused severe lattice damage that

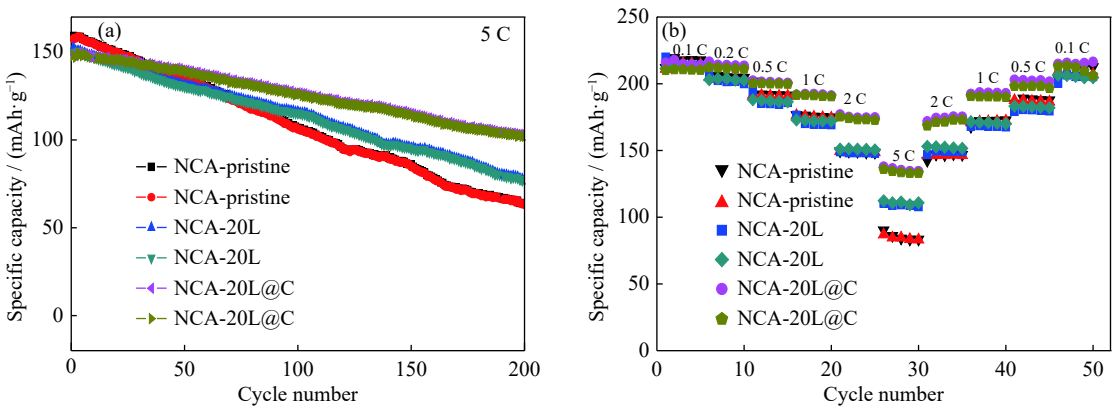

Fig. 4. (a) Cycling performance of NCA-pristine, NCA-20L, and NCA-20L@C at 5 C; (b) rating performance from 0.1 up to 5 C and down to 0.1 C. The voltage ranged from 2.7 to 4.3 V (1 C = 200 mA·g^{-1}).

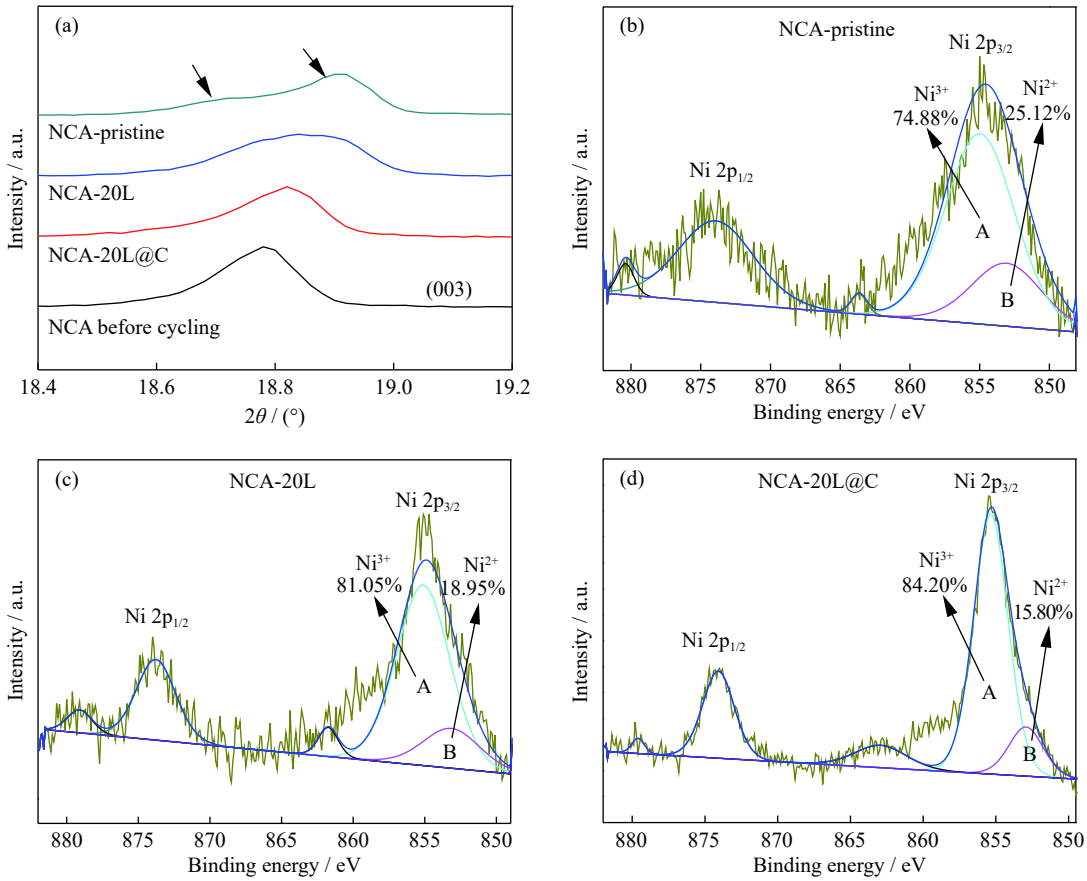

Fig. 5. (a) Evolution of the (003) diffraction peak of the cathodes before and after 200 cycles at 5 C. Deconvoluted XPS spectra of Ni 2p taken from the surface of (b) NCA-pristine, (c) NCA-20L, and (d) NCA-20L@C after 200 cycles at 5 C.

is continuous and forms a domain-boundary-like region. The spinel phase is maintained with a distinct lattice fringe spacing of 0.46 nm, which corresponds to the (111) crystalline plane of the H_2 phase. The representative regions in Fig. 6(a) were observed (Fig. 6(a1)) and denoted regions I, II, and III. The damaged region (II) consists of serial edge dislocations (⊥) that form a dislocation wall. The formation of a dense dislocation wall is considered an important cause of the domain boundary propagation. The formation of domains in the ternary cathode materials remains under much investigation [16]. This region is also a so-called "broken atomic region" according to Yang and Xia [21]. This phenomenon originated from the accumulation of contraction and expansion of the unit cell volume, which is induced by the phase transition between H_2 and H_3 during repeated delithiation and lithiation. In Region III, faint bright spots, as shown by the yellow circles, are apparent between the crystalline planes, indicating that a large amount of TM ions (Ni^{2+}) has diffused to the Li^+ vacancy [22]. Severe cation mixing leads to aggravated lattice distortion and structure degradation, which indicates the occurrence of the irreversible phase transition of H_3. The lattice spacing narrows because of the insertion of the ordered TM atom layers in the interstitial Li sites, which is the reason for the generation of the rock-salt phase. As a result, in the surface region of NCA (Fig. 6(b)), the irreversible rock-salt phase (NiO) is formed. The formation of the NiO phase is a direct result of highly ordered cation mixing (III in Fig. 6(a1). The lattice distance is 0.21 nm, which corresponds to the $(200)_C$ crystalline plane of the rock-salt phase (Fm-3m). A continuous NiO phase "shell" on the NCA particles results in severe irreversible capacity loss in the NCA cathode, as reported previously [57–59].

The structure of NCA in NCA-20L@C after high-rate cycling was observed using HRTEM and is shown in Fig. 7. Figs. 7(a) and 7(b) show the two typical regions from the interior of the NCA particle (Fig. 7(a)) to the surface (Fig. 7(b)). In Fig. 7(a), the well-ordered layered structure with a lattice distance of 0.47 nm is maintained, and no structural damage occurs in the bulk, which differs from the localized structure degradation of NCA-pristine (Fig. 6). The layered crystalline plane $(003)_R$ with an R-3m symmetry can be further verified by the corresponding FFT shown in the inset of Fig. 7(a). Fig. 7(b) shows the structure on the surface region of NCA in NCA-20L@C. The clear lattice fringes corresponding to the (111) plane of the spinel phase demonstrate that most regions maintain the spinel structure on the surface. The two broken atomic planes in Fig. 7(b1) resulted in the formation of adjacent edge dislocations (⊥). The lattice

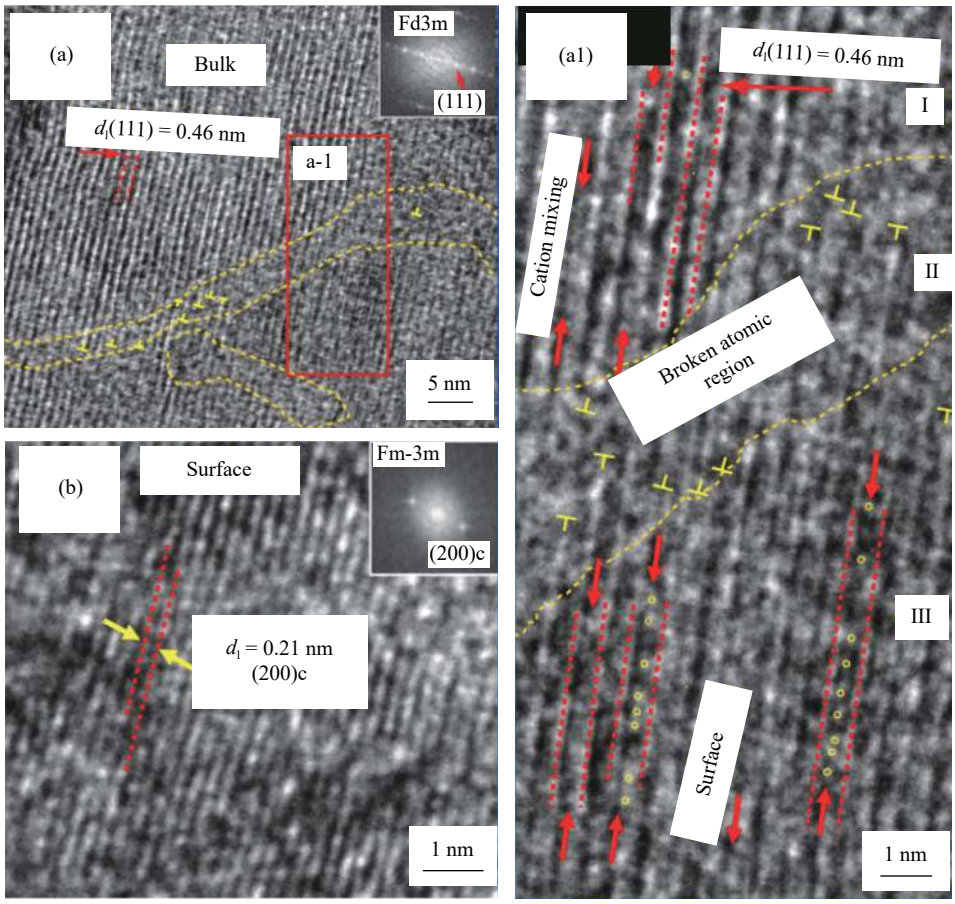

Fig. 6. HRTEM images and fast Fourier transform (FFT) patterns (insets) of NCA-pristine after cycling: (a) HRTEM image from a region inside the NCA particle; (a1) magnified image of the selected region of the rectangle in (a); (b) HRTEM image from the surface region of NCA. The "d_l" refers to the lattice distance of NCA.

damage is limited to the scale of two atom layers. As seen in Figs. 6(a) and 6(a1), the phase transition (H_2 and H_3) in NCA-pristine caused severe lattice damage, where the dense edge dislocations form a domain boundary and propagate inside the NCA bulk. The cation mixing of Li–Ni is shown in Fig. 7(b2), as indicated by the yellow circles. The formation of Li^+/Ni^{2+} mixing is limited within a scale of several sub-cells, and the resultant change in the lattice spacing occurs accordingly [60]. A highly ordered cation mixing region is formed locally in the surface region (2−4 nm), as shown in Fig. 7(b3). In the selected region of Fig. 7(b3), the highly ordered occupation generates distorted rock-salt phase "pitting." The lattice spacing varied from 0.22 to 0.24 nm, which corresponds to the (111) plane spacing of NiO. With the modification of LLTO@C, the generation of the rock-salt phase was limited and localized on the surface.

A mechanism based on the coupling effect of the Li ions and electron conductivities is illustrated in Fig. 8. As required by the typical cycling reaction of Ni ions, the transport of Li^+ and electrons is necessary for obtaining the full reversibility of $Ni^{2+/3+}$. However, the transport of Li cations and electrons relies on different systems. In the cathode, PDVF binder provides a low conductivity to Li^+, while the electrical conductivity depends on the discontinuous carbon components [61]. The modification of the LLTO@C core-shell nanofibers in PVDF can set up a series of coupling pathways for Li^+ and e−, as illustrated in Fig. 8. The blue and purple arrows indicate the conductivities of Li^+ and electrons in the core and sheath of LLTO@C, respectively. During the lithiation, the supply of Li ions is boosted by LLTO, which helps Li^+ to fully occupy the interstitial sites and promotes Ni cation migration back to the lattice sites [27]. The charge of the Li ions can also be compensated by the external circuit because of their "rocking chair" effect. As indicated in Figs. 2 and 3, the LLTO@C improves the diffusion kinetics in the NCA cathode, which can promote the stabilization of the layer structure, as previously reported [39,61–63]. However, the TM cations must obtain charge compensation from the local environment. The carbon layer on LLTO fibers provides a continuous, electrically conductive path beyond dispersed carbon black, which helps to promote the Ni transition from the +2 state to the +3 state. As a result, NCA-20L@C tends to retain its initial layer structure, rather than the rock-salt state.

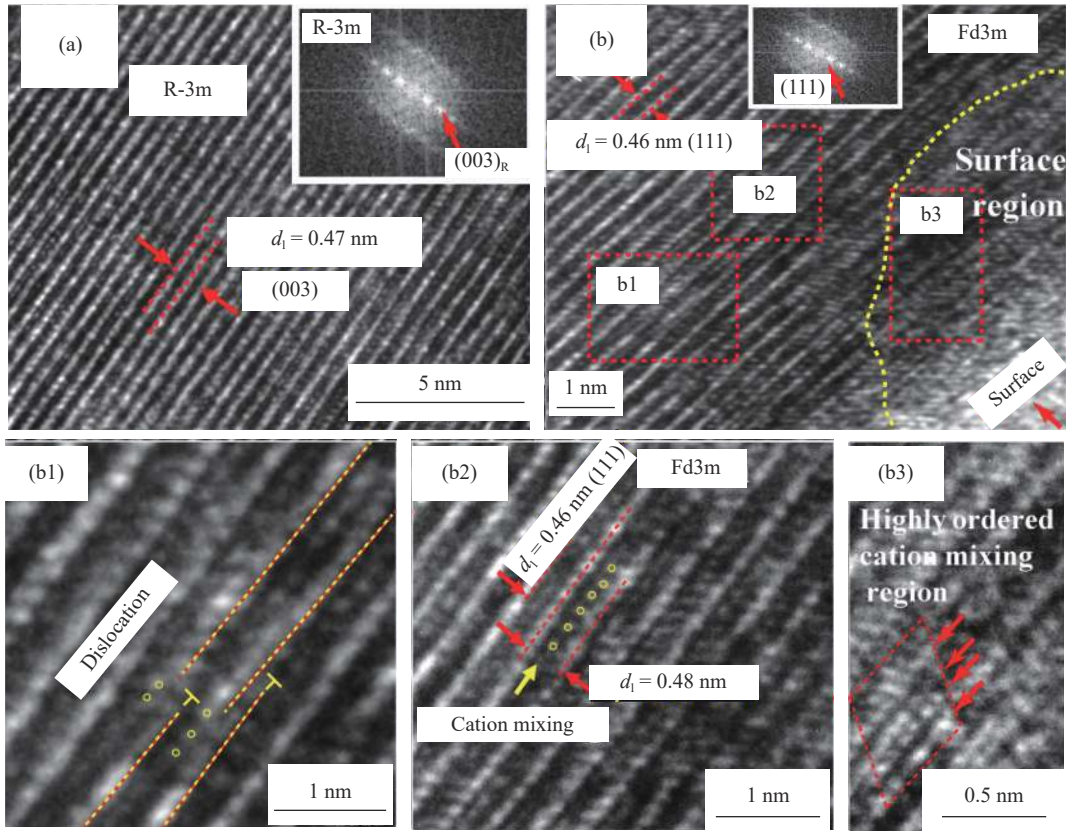

Fig. 7. HRTEM images and the corresponding FFT (inset) obtained from the bulk (a) to the surface (b) of NCA in NCA-20L@C. Images (b1), (b2), and (b3) present magnifications of the three regions shown in image (b). The "d_1" refers to the lattice distance of NCA.

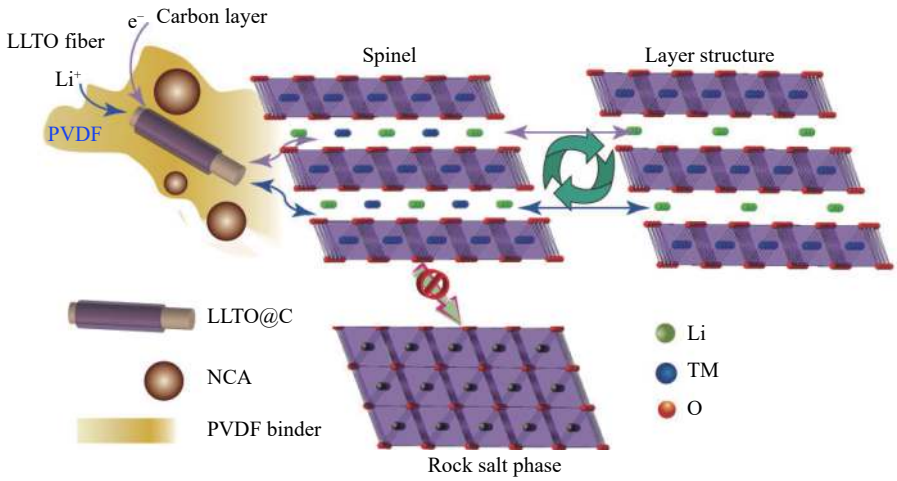

Fig. 8. Schematic of the structure of the coupling mechanism of the co-conduction of Li ions and electrons in the NCA cathode.

4. Conclusion

The coupling effect of the Li cation and electron conductivities was revealed by introducing LLTO and LLTO@C into the PVDF binder of an NCA cathode. The EIS measurements before and after cycling demonstrate the promotion of the Li conductivity. Interestingly, the electrical conductivity of the NCA-20L@C cathode before cycling was almost identical to that after cycling. The surface diffusion coefficient of Li^+ was improved. The EIS and CV curves verified the decreased polarization and enhanced diffusivity. By modification with LLTO@C, the capacity retention of the NCA-20L@C cell increased from 40.2%, which is the capacity retention of pristine NCA, to 68.9% at 5 C after 200

cycles. The XPS results confirm the suppression of the formation of Ni^{2+} on the surface of NCA in NCA-20L@C. The TEM images of NCA in NCA-20L@C demonstrate that cation mixing was alleviated and the structural deterioration was inhibited. The irreversible phase transition only occurred locally on the surface. In contrast, the pristine NCA showed a continuous rock-salt layer on the surface. In the interior of NCA, a broken lattice region formed, which was accompanied by the formation of dense dislocation walls, indicating a severe phase transition between H_2 and H_3. The coupling effect was emphasized by the change in the cathode's electrochemical performance with the addition of LLTO@C and LLTO. The coupling of the Li ions and electrons in NCA cathodes provides a new approach for optimizing the kinetics of microenvironments, which is a promising parallel strategy to the "core-shell" structure.

Acknowledgements

This work was financially supported by the National Natural Science Foundation of China (Nos. 51571182 and 51001091), the Fundamental Research Program from the Ministry of Science and Technology of China (No. 2014CB931704), the Program for Innovative Research Team (in Science and Technology) in University of Henan Province (No. 21IRTSTHN003). This work was also partially supported by the Provincial Scientific Research Program of Henan (No. 182102310815).

References

[1] L.F. Guo, S.Y. Zhang, J. Xie, D. Zhen, Y. Jin, K.Y. Wan, D.G. Zhuang, W.Q. Zheng, and X.B. Zhao, Controlled synthesis of nanosized Si by magnesiothermic reduction from diatomite as anode material for Li-ion batteries, *Int. J. Miner. Metall. Mater.*, 27(2020), No. 4, p. 515.

[2] D.B. Li, L.Y. Cao, C.D. Liu, G.Q. Cao, J.H. Hu, J.B. Chen, and G.S. Shao, A designer fast Li-ion conductor $Li_{6.25}PS_{5.25}Cl_{0.75}$ and its contribution to the polyethylene oxide based electrolyte, *Appl. Surf. Sci.*, 493(2019), p. 1326.

[3] J.B. Goodenough, Electrochemical energy storage in a sustainable modern society, *Energy Environ. Sci.*, 7(2014), No. 1, p. 14.

[4] Y. Han, S.Y. Liu, L. Cui, L. Xu, J. Xie, X.K. Xia, W.K. Hao, B. Wang, H. Li, and J. Gao, Graphene-immobilized flower-like Ni_3S_2 nanoflakes as a stable binder-free anode material for sodium-ion batteries, *Int. J. Miner. Metall. Mater.*, 25(2018), No. 1, p. 88.

[5] Y.M. Sun, N. Liu, and Y. Cui, Promises and challenges of nanomaterials for lithium-based rechargeable batteries, *Nat. Energy*, 1(2016), No. 7, art. No. 16071.

[6] G.Q. Cao, Y.Y. Ren, K.K. Wu, H.H. Yao, J.H. Hu, G.S. Shao, and G.H. Yuan, Life extension strategy and research progress of zirconium alloy cladding applied to light water reactors, *Surf. Technol.*, 48(2019), No. 11, p. 69.

[7] G.Q. Cao, L. Yang, G.H. Yuan, J.H. Hu, G.S. Shao, and L. Yan, Chemical diversity of iron species and structure evolution during the oxidation of C14 laves phase $Zr(Fe,Nb)_2$ in subcritical environment, *Corros. Sci.*, 162(2020), art. No. 108218.

[8] A. Iqbal, L. Chen, Y. Chen, Y.X. Gao, F. Chen, and D.C. Li, Lithium-ion full cell with high energy density using nickel-rich $LiNi_{0.8}Co_{0.1}Mn_{0.1}O_2$ cathode and SiO–C composite anode, *Int. J. Miner. Metall. Mater.*, 25(2018), No. 12, p. 1473.

[9] L.P. Wang, G. Chen, Q.X. Shen, G.M. Li, S.Y. Guan, and B. Li, Direct electrodeposition of ionic liquid-based template-free SnCo alloy nanowires as an anode for Li-ion batteries, *Int. J. Miner. Metall. Mater.*, 25(2018), No. 9, p. 1027.

[10] N.V. Faenza, N. Pereira, D.M. Halat, J. Vinckeviciute, L. Bruce, M.D. Radin, P. Mukherjee, F. Badway, A. Halajko, F. Cosandey, C.P. Grey, A. Van der Ven, and G.G. Amatucci, Phase evolution and degradation modes of R3-m $Li_xNi_{1-y-z}Co_yAl_zO_2$ electrodes cycled near complete delithiation, *Chem. Mater.*, 30(2018), No. 21, p. 7545.

[11] P.Y. Hou, J.M. Yin, M. Ding, J.Z. Huang, and X.J. Xu, Surface/interfacial structure and chemistry of high-energy nickel-rich layered oxide cathodes: Advances and perspectives, *Small*, 13(2017), No. 45, art. No. 1701802.

[12] S.M. Bak, K.W. Nam, W.Y. Chang, X.Q. Yu, E.Y. Hu, S. Hwang, E.A. Stach, K.B. Kim, K.Y. Chung, and X.Q. Yang, Correlating structural changes and gas evolution during the thermal decomposition of charged $Li_xNi_{0.8}Co_{0.15}Al_{0.05}O_2$ cathode materials, *Chem. Mater.*, 25(2013), No. 3, p. 337.

[13] K.L. Cheng, D.B. Mu, B.R Wu, L. Wang, Y. Jiang, and R. Wang, Electrochemical performance of a nickel-rich $LiNi_{0.6}Co_{0.2}Mn_{0.2}O_2$ cathode material for lithium-ion batteries under different cut-off voltages, *Int. J. Miner. Metall. Mater.*, 24(2017), No. 3, p. 342.

[14] U.H. Kim, D.W. Jun, K.J. Park, Q. Zhang, P. Kaghazchi, D. Aurbach, D.T. Major, G. Goobes, M. Dixit, N. Leifer, C.M. Wang, P. Yan, D. Ahn, K.H. Kim, C.S. Yoon, and Y.K. Sun, Pushing the limit of layered transition metal oxide cathodes for high-energy density rechargeable Li ion batteries, *Energy Environ. Sci.*, 11(2018), No. 5, p. 1271.

[15] K.K. Lee, W.S. Yoon, K.B. Kim, K.Y. Lee, and S.T. Hong, Thermal behavior and the decomposition mechanism of electrochemically delithiated $Li_{1-x}NiO_2$, *J. Power Sources*, 97-98(2001), p. 321.

[16] S. Hwang, W. Chang, S.M. Kim, D. Su, D.H. Kim, J.Y. Lee, K.Y. Chung, and E.A. Stach, Investigation of changes in the surface structure of $Li_xNi_{0.8}Co_{0.15}Al_{0.05}O_2$ cathode materials induced by the initial charge, *Chem. Mater.*, 26(2014), No. 2, p. 1084.

[17] H.L. Zhang, F. Omenya, M.S. Whittingham, C.M. Wang, and G.W. Zhou, Formation of an anti-core-shell structure in layered oxide cathodes for Li-ion batteries, *ACS Energy Lett.*, 2(2017), No. 11, p. 2598.

[18] S.H. Lee, S. Lee, B.S. Jin, and H.S. Kim, Preparation and electrochemical performances of Ni-rich $LiNi_{0.91}Co_{0.06}Mn_{0.03}O_2$ cathode for high-energy LIBs, *Int. J. Hydrogen Energy*, 44(2019), No. 26, p. 13684.

[19] D.P. Abraham, R.D. Twesten, M. Balasubramanian, I. Petrov, J. McBreen, and K. Amine, Surface changes on $LiNi_{0.8}Co_{0.2}O_2$ particles during testing of high-power lithium-ion cells, *Electrochem. Commun.*, 4(2002), No. 8, p. 620.

[20] J.K. Zhao, Z.X. Wang, J.X. Wang, H.J Guo, X.H. Li, W.H. Gui, N. Chen, and G.H. Yan, Anchoring K^+ in Li^+ sites of $LiNi_{0.8}Co_{0.15}Al_{0.05}O_2$ cathode material to suppress its structural degradation during high-voltage cycling, *Energy Technol.*, 6(2018), No. 12, p. 2358.

[21] J. Yang and Y.Y. Xia, Suppressing the phase transition of the

layered Ni-rich oxide cathode during high-voltage cycling by introducing low-content Li_2MnO_3, *ACS Appl. Mater. Interfaces*, 8(2016), No. 2, p. 1297.

[22] C.C. Fu, G.S. Li, D. Luo, Q. Li, J.M. Fan, and L.P. Li, Nickel-rich layered microspheres cathodes: lithium/nickel disordering and electrochemical performance, *ACS Appl. Mater. Interfaces*, 6(2014), No. 18, p. 15822.

[23] B.S. Liu, Z.B. Wang, F.D. Yu, Y. Xue, G.J. Wang, Y. Zhang, and Y.X. Zhou, Facile strategy of NCA cation mixing regulation and its effect on electrochemical performance, *RSC Adv.*, 6(2016), No. 110, p. 108558.

[24] T. Hayashi, J. Okada, E. Toda, R. Kuzuo, N. Oshimura, N. Kuwata, and J. Kawamura, Degradation mechanism of $LiNi_{0.82}Co_{0.15}Al_{0.03}O_2$ positive electrodes of a lithium-ion battery by a long-term cycling test, *J. Electrochem. Soc.*, 161(2014), No. 6, p. A1007.

[25] S. Sharifi-Asl, F.A. Soto, A. Nie, Y.F. Yuan, H. Asayesh-Ardakani, T. Foroozan, V. Yurkiv, B. Song, F. Mashayek, R.F. Klie, Amine, J. Lu, P.B. Balbuena, and R. Shahbazian-Yassar, Facet-dependent thermal instability in $LiCoO_2$, *Nano Lett.*, 17(2017), No. 4, p. 2165.

[26] J.F. Zhang, J.Y. Zhang, X. Ou, C.H. Wang, C.L. Peng, and B. Zhang, Enhancing high-voltage performance of Ni-rich cathode by surface modification of self-assembled NASICON fast ionic conductor $LiZr_2(PO_4)_3$, *ACS Appl. Mater. Interfaces*, 11(2019), No. 17, p. 15507.

[27] C.L. Xu, W. Xiang, Z.G. Wu, Y.C. Li, Y.D. Xu, W.B. Hua, X.D. Guo, X.B. Zhang, and B.H. Zhong, A comparative study of crystalline and amorphous $Li_{0.5}La_{0.5}TiO_3$ as surface coating layers to enhance the electrochemical performance of $LiNi_{0.815}Co0.15Al_{0.035}O_2$ cathode, *J. Alloys Compd.*, 740(2018), p. 428.

[28] Y.Y. Ren, H.H. Yao, J.H. Hu, G.Q. Cao, J.J. Tian, and J.M. Pan, Evolution of "spinodal decomposition"-like structures during the oxidation of $Zr(Fe,Nb)_2$ under subcritical environment, *Scripta Mater.*, 187(2020), p. 107.

[29] S. Ito, S. Fujiki, T. Yamada, Y. Aihara, Y. Park, T.Y. Kim, S.W. Baek, J.M. Lee, S. Doo, and N. Machida, A rocking chair type all-solid-state lithium ion battery adopting Li_2O–ZrO_2 coated $LiNi_{0.8}Co_{0.15}Al_{0.05}O_2$ and a sulfide based electrolyte, *J. Power Sources*, 248(2014), p. 943.

[30] J.G. Duan, C. Wu, Y.B. Cao, K. Du, Z.D. Peng, and G.R. Hu, Enhanced electrochemical performance and thermal stability of $LiNi_{0.80}Co_{0.15}Al_{0.05}O_2$ via nano-sized $LiMnPO_4$ coating, *Electrochim. Acta*, 221(2016), p. 14.

[31] E.Y. Zhao, M.M. Chen, Z.B. Hu, D.F. Chen, L.M. Yang, and X.L. Xiao, Improved cycle stability of high-capacity Ni-rich $LiNi_{0.8}Mn_{0.1}Co_{0.1}O_2$ at high cut-off voltage by Li_2SiO_3 coating, *J. Power Sources*, 343(2017), p. 345.

[32] X.D. Jiang, Y. Wei, X.H. Yu, P. Dong, Y.J. Zhang, Y.N. Zhang, and J.X. Liu, $CeVO_4$-coated $LiNi_{0.6}Co_{0.2}Mn_{0.2}O_2$ as positive material: Towards the excellent electrochemical performance at normal and high temperature, *J. Mater. Sci. Mater. Electron.*, 29(2018), No. 18, p. 15869.

[33] Y.Q. Huang, Y.H. Huang, and X.L. Hu, Enhanced electrochemical performance of $LiNi_{0.8}Co_{0.15}Al_{0.05}O_2$ by nanoscale surface modification with Co_3O_4, *Electrochim. Acta*, 231(2017), p. 294.

[34] S.M. Sun, T. Liu, Q.H. Niu, X.L. Sun, D.P. Song, H. Liu, X.X. Zhou, T. Ohsaka, and J.F. Wu, Improvement of superior cycle performance of $LiNi_{0.8}Co_{0.15}Al_{0.05}O_2$ cathode for lithium-ion batteries by multiple compound modifications, *J. Electroanal. Chem.*, 838(2019), p. 178.

[35] X.S. He, C.Y. Du, B. Shen, C. Chen, X. Xu, Y.J. Wang, P.J. Zuo, Y.L. Ma, X.Q. Cheng, and G.P. Yin, Electronically conductive Sb-doped SnO_2 nanoparticles coated $LiNi_{0.8}Co_{0.15}Al_{0.05}O_2$ cathode material with enhanced electrochemical properties for Li-ion batteries, *Electrochim. Acta*, 236(2017), p. 273.

[36] C.D. Liu, G.Q. Cao, Z.H. Wu, J.H. Hu, H.Y. Wang, and G.S. Shao, Surficial structure retention mechanism for $LiNi_{0.8}Co_{0.15}Al_{0.05}O_2$ in a full gradient cathode, *ACS Appl. Mater. Interfaces*, 11(2019), No. 35, p. 31991.

[37] F.Y. Fan, W.H. Woodford, Z. Li, N. Baram, K.C. Smith, A. Helal, G.H. Mckinley, W.C. Carter, and Y.M. Chiang, Polysulfide flow batteries enabled by percolating nanoscale conductor networks, *Nano Lett.*, 14(2014), No. 4, p. 2210.

[38] Y.K. Wang, R.F. Zhang, J. Chen, H. Wu, S.Y. Lu, K. Wang, H.L. Li, C.J. Harris, K. Xi, R.V. Kumar, and S.J. Ding, Enhancing catalytic activity of titanium oxide in lithium–sulfur batteries by band engineering, *Adv. Energy Mater.*, 9(2019), No. 24, art. No. 1900953.

[39] R. Amin, D.B. Ravnsbaek, and Y.M. Chiang, Characterization of electronic and ionic transport in $Li_{1-x}Ni_{0.8}Co_{0.15}Al_{0.05}O_2$ (NCA), *J. Electrochem. Soc.*, 162(2015), No. 7, p. A1163.

[40] H. Yuan, J.Q. Huang, H.J. Peng, M.M. Titirici, R. Xiang, R.J Chen, Q.B. Liu, and Q. Zhang, A review of functional binders in lithium–sulfur batteries, *Adv. Energy Mater.*, 8(2018), No. 31, art. No. 1802107.

[41] X.N. He, S.Y. Li, G.Q. Cao, J.H. Hu, J.H. Zhang, R. Qiao, J.M. Pan, and G.S. Shao, *In situ* atomic-scale engineering of the chemistry and structure of the grain boundaries region of $Li_{3x}La_{2/3-x}TiO_3$, *Scripta Mater.*, 185(2020), p. 134.

[42] T. Yang, Y. Li, and C.K. Chan, Enhanced lithium ion conductivity in lithium lanthanum titanate solid electrolyte nanowires prepared by electrospinning, *J. Power Sources*, 287(2015), p. 164.

[43] W.E. Teo and S. Ramakrishna, A review on electrospinning design and nanofibre assemblies, *Nanotechnology*, 17(2006), No. 14, p. R89.

[44] W. Liu, S.W. Lee, D.C. Lin, F.F. Shi, S. Wang, A.D Sendek, and Y. Cui, Enhancing ionic conductivity in composite polymer electrolytes with well-aligned ceramic nanowires, *Nat. Energy*, 2(2017), No. 5, art. No. 17035.

[45] N.C. Zheng, X.F. Li, S. Yan, Q. Wang, R. Qiao, J.H. Hu, J.J. Fan, G.Q. Cao, and G.S. Shao, Nano-porous Hollow $Li_{0.5}La_{0.5}TiO_3$ spheres and electronic structure modulation for ultra-fast H_2S detection, *J. Mater. Chem. A*, 8(2020), No. 5, p. 2376.

[46] L. Fan, S.Y. Wei, S.Y. Li, Q. Li, and Y.Y. Lu, Recent progress of the solid-state electrolytes for high-energy metal-based batteries, *Adv. Energy Mater.*, 8(2018), No. 11, art. No. 1702657.

[47] Q. Wang, J.H. Zhang, X.N. He, G.Q. Cao, J.H. Hu, J.M. Pan, and G.S. Shao, Synergistic effect of cation ordered structure and grain boundary engineering on long-term cycling of $Li_{0.35}La_{0.55}TiO_3$-based solid batteries, *J. Eur. Ceram. Soc.*, 39(2019), No. 11, p. 3332.

[48] J.H. Hu, P. Wang, P.P. Liu, G.Q. Cao, Q. Wang, M. Wei, J. Mao, C.H. Liang, and G.Q. Shao, *In situ* fabrication of nano porous NiO-capped Ni_3P film as anode for Li-ion battery with different lithiation path and significantly enhanced electrochemical performance, *Electrochim. Acta*, 220(2016), p. 258.

[49] H.J. Noh, S.G. Youn, C.S. Yoon, and Y.K. Sun, Comparison of the structural and electrochemical properties of layered $Li[Ni_xCo_yMn_z]O_2$ (x = 1/3, 0.5, 0.6, 0.7, 0.8 and 0.85) cathode material for lithium-ion batteries, *J. Power Sources*, 233(2013), p. 121.

[50] L. Croguennec, C. Pouillerie, and C. Delmas, Structural characterisation of new metastable NiO_2 phases, *Solid State Ionics*, 135(2000), No. 1-4, p. 259.

[51] P. Wang, J.H. Hu, G.Q. Cao, S.L. Zhang, P. Zhang, C.H. Liang, Z. Wang, and G.S. Shao, Suppression on allotropic transformation of Sn planar anode with enhanced electrochemical performance, *Appl. Surf. Sci.*, 435(2018), p. 1150.

[52] J.H. Hu, L. Yang, G.Q. Cao, Y.F. Yun, G.H. Yuan, Q. Yue, and G.S. Shao, On the oxidation behavior of $(Zr,Nb)_2Fe$ under simulated nuclear reactor conditions, *Corros. Sci.*, 112(2016), p. 718.

[53] W. Li, J.N. Reimers, and J.R. Dahn, *In situ* X-ray diffraction and electrochemical studies of $Li_{1-x}NiO_2$, *Solid State Ionics*, 67(1993), No. 1-2, p. 123.

[54] S.Q. Cao, Q.J. Wang, J.H. Hu, Z.Y. Fu, K.F. Bai, G.S. Shao, and G.Q. Cao, Dominant growth of higher manganese silicide film on Si substrate by introducing a Si oxide capping layer, *J. Alloys Compd.*, 740(2018), p. 541.

[55] Y. Cho, P. Oh, and J. Cho, A new type of protective surface layer for high-capacity Ni-based cathode materials: Nanoscaled surface pillaring layer, *Nano Lett.*, 13(2013), No. 3, p. 1145.

[56] Z.J. Peng, G.W. Yang, F.Q. Li, Z.H. Zhu, and Z.Y. Liu, Improving the cathode properties of Ni-rich $LiNi_{0.6}Co_{0.2}Mn_{0.2}O_2$ at high voltages under 5 C by Li_2SiO_3 coating and Si^{4+} doping, *J. Alloys Compd.*, 762(2018), p. 827.

[57] S.J. Zheng, R. Huang, Y. Makimura, Y. Ukyo, C.A.J. Fisher, T. Hirayama, and Y. Ikuhara, Microstructural changes in $LiNi_{0.8}Co_{0.15}Al_{0.05}O_2$ positive electrode material during the first cycle, *J. Electrochem. Soc.*, 158(2011), No. 4, p. A357.

[58] H. Setiawan, H.T.B. Murti Petrus, and I. Perdana1, Reaction kinetics modeling for lithium and cobalt recovery from spent lithium-ion batteries using acetic acid, *Int. J. Miner. Metall. Mater.*, 26(2019), No. 1, p. 98.

[59] G.Q. Cao, Y.F. Yun, H.J. Xu, G.H. Yuan, J.H. Hu, and G.S. Shao, A mechanism assessment for the anti-corrosion of zirconia coating under the condition of subcritical water corrosion, *Corros. Sci.*, 152(2019), p. 54.

[60] B. Xu, C.R. Fell, M.F. Chi, and Y.S. Meng, Identifying surface structural changes in layered Li-excess nickel manganese oxides in high voltage lithium ion batteries: A joint experimental and theoretical study, *Energ. Environ. Sci.*, 4(2011), No. 6, p. 2223.

[61] Q. Wang, X.F. Li, X.N. He, L.Y. Cao, G.Q. Cao, H.J. Xu, J.H. Hu, and G.S. Shao, Two-pronged approach to regulate Li etching for a stable anode, *J. Power Sources*, 455(2020), art. No. 227988.

[62] D.N. Qian, B. Xu, H.M. Cho, T. Hatsukade, K.J. Carroll, and Y.S. Meng, Lithium lanthanum titanium oxides: A fast ionic conductive coating for lithium-ion battery cathodes, *Chem. Mater.*, 24(2012), No. 14, p. 2744.

[63] H.Y. Guan, F. Lian, Y. Ren, Y. Wen, X.R. Pan, and J.L Sun, Comparative study of different membranes as separators for rechargeable lithium-ion batteries, *Int. J. Miner. Metall. Mater.*, 20(2013), No. 6, p. 598.